

Calculation of Crater Shape in Pulsed Laser Ablation of Hard Tissues

Boris Majaron, PhD^{1*} and Matjaž Lukač, PhD^{1,2}

¹Jožef Stefan Institute, SI-1000 Ljubljana, Slovenia

²Slovenian Development Corporation, SI-1000 Ljubljana, Slovenia

Background and Objective: An expression describing the ablation crater shape as a function of lateral fluence distribution has been derived in a recent paper by Ostertag et al. [Lasers Surg Med 1997; 21:384–394].

Study Design/Materials and Methods: The ablation model presented therein is improved by taking into account the influence of the ablation front inclination on the ablation dynamics.

Results: The resulting crater profiles deviate from the previously predicted ones (which reflect the Gaussian fluence distribution of the impinging laser beam) progressively with increasing pulse fluence.

Conclusion: The ablation front inclination must be taken into account to predict the ablation crater shapes and volumes correctly. Lasers Surg. Med. 24:55–60, 1999. © 1999 Wiley-Liss, Inc.

Key words: ablation dynamics; ablation modeling; crater profile; mid-infrared laser ablation; repetitive pulse sequence.

INTRODUCTION

In an appendix to a recent paper [1], Ostertag et al. presented an analytical model of mid-infrared laser ablation process that produced a simple expression for the ablation crater shape as a function of the fluence distribution within the laser pulse. According to their result, the crater profile expressed in polar coordinates as $d(r, \phi)$ is a replica of the fluence distribution $F(r, \phi)$ cut off at the base to account for the fluence amount needed to achieve the ablation threshold (F_v):

$$d(r, \phi) = \frac{1}{\alpha} \left(\frac{F(r, \phi)}{F_v} - 1 \right). \quad (1)$$

In equation (1), α stands for the tissue absorption coefficient at the laser wavelength. The derivation quoted above is certainly exact in describing the ablation of half-infinite tissue by a laterally infinite plane wave impinging perpendicularly on its flat surface. Accordingly, a reduction of (1) to one dimension,

$$d = \frac{1}{\alpha} \left(\frac{F}{F_v} - 1 \right), \quad (2)$$

is widely used to predict or analyze the depths of ablation craters, which are often shallow in comparison with the beam diameter, and have a flat bottom.

In general, however, spatial nonhomogeneity of the laser intensity causes the ablation front to incline from the normal to the beam axis, which in turn diminishes the ablation velocity. As we show in the following paragraphs, this results in crater shapes that deviate from the pulse fluence distribution, especially at higher pulse fluence values. Consequently, crater volumes and ablated mass calculated from (1) are systematically overestimated, which is progressively more pronounced with increasing pulse fluence. The influence of ablation front inclination, which was completely disregarded by Ostertag et al. [1], thus limits the

Contract grant sponsor: Slovenian Ministry of Science and Technology.

*Correspondence to: Boris Majaron, PhD, Jožef Stefan Institute, p.p. 3000, SI-1001 Ljubljana, Slovenia. E-mail: boris.majaron@ijs.si

Accepted 10 September 1998

validity of (1) to shallow craters with low crater wall inclinations.

Because we are unable to solve the corrected ablation model analytically, approximate numerical solutions are presented for a temporally constant laser pulse with a Gaussian intensity profile. For further resemblance with the 6.0- μm emission of the free-electron laser (FEL) discussed in [1], a pulse duration of $\tau = 5 \mu\text{sec}$ and a beam waist radius of $w = 0.54 \text{ mm}$ (0.65 mm full width at half maximum) are used in the numerical evaluations. Likewise, the dentin absorption coefficient is set to $\alpha = 200 \text{ mm}^{-1}$ and the specific heat of ablation is set to $e_v = 2.5 \text{ J/mm}^3$, as determined experimentally in [1].

Note that the whole discussion applies exclusively to situations where no heat diffuses from the interaction volume during the laser pulse. In the experiments described in [1], for example, this was ensured by the pulse duration significantly shorter than the thermal relaxation time. The latter can be estimated from thermal diffusivity of dentin ($D = 1.1 \times 10^{-7} \text{ m}^2/\text{sec}$) to $\tau_r = 1/(D \alpha^2) \sim 110 \mu\text{sec}$. In addition, the laser radiation should not be absorbed or scattered by the ablation debris, which is called debris screening [2–4]. This is discussed in more detail at the end of the article, after an analysis of some specifics of ablation with repetitively pulsed laser irradiation.

However, the fact that the FEL emission consists of regularly spaced 1-psec micropulses is effectively irrelevant, provided that the dominant ablation mechanism is thermally initiated and the specific heat of ablation e_v can be introduced. This quantity is sometimes referred to as evaporation energy density, although there are numerous indications that the mid-infrared laser ablation of tissue is not a purely evaporative process but also involves mechanical effects [5–8]. This thermomechanical ablation regime applies until individual micropulses can initiate additional ablation mechanisms such as optical breakdown or spallation.

INFLUENCE OF THE ABLATION FRONT INCLINATION

Inclination of the ablation front causes the impinging radiation intensity to be distributed over a larger surface area, thus reducing the local energy deposition rate ($\partial e/\partial t$). For the clarity of the argument, we limit further discussion to temporally constant laser pulses with cylindrical

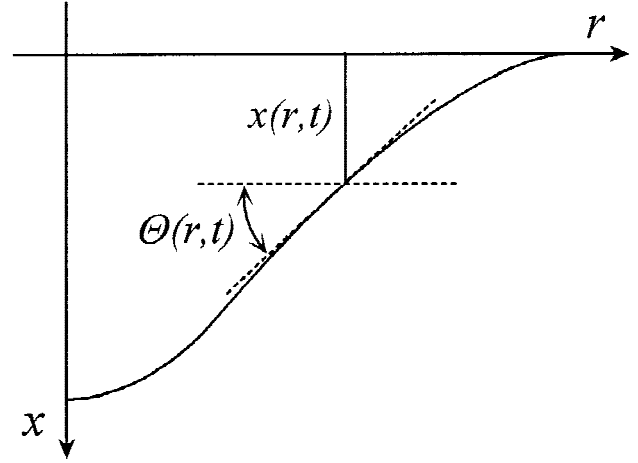


Fig. 1. Schematic illustration of an axially symmetrical ablation crater whose profile at a general time t is described by function $x(r, t)$. The x axis runs into the irradiated tissue along the symmetry axis of the laser beam, and the r axis runs radially along the tissue surface. The function $\theta(r, t)$ marks the crater wall inclination at a general radial position r and time t .

symmetry. By using the same variable notation as in [1] and introducing $\theta(r, t)$ to represent the ablation front inclination relative to the initial tissue surface (see Fig. 1), dynamics of the ablation front $x(r, t)$ is correctly described by

$$\frac{\partial e(z, t)}{\partial t} - \frac{\partial x(r, t)}{\partial t} \frac{\partial e(z, t)}{\partial z} = \frac{\alpha}{\tau} F(r) e^{-\alpha z} \cos \theta(r, t). \quad (3)$$

After inserting the ansatz $e(z, t) = e_v \exp(-\alpha z)$ and expressing $\cos \theta$ with $\tan \theta$, which in turn is equal to the gradient of the crater profile $\partial x(r, t)/\partial r$, we finally obtain the corrected ablation dynamics equation:

$$\frac{\partial x(r, t)}{\partial t} = \frac{F(r)}{\tau e_v} \left[1 + \left(\frac{\partial x(r, t)}{\partial r} \right)^2 \right]^{-\frac{1}{2}}. \quad (4)$$

Because we are unable to solve equation (4) analytically, an approximate solution is calculated below by using an iterative method. First, a zero-order approximation of the crater profile evolution $x_0(r, t)$ is calculated by neglecting the—supposedly small—ablation front inclination term in (4) and integrating the remaining ordinary differential equation from the ablation set-up time $t_v(r)$ to a general time t :

$$x_0(r, t) = \frac{F(r)}{\tau e_v} \int_{t_v(r)}^t dt' = \frac{F(r)}{\tau e_v} t - \frac{1}{\alpha}. \quad (5)$$

The calculation thus far is actually exactly the same as that in [1], so it is not surprising that the 0th approximation of the final crater profile $d_0(r)$ obtained by inserting the pulse duration τ for t in (5) matches the expression (1). Note that the usual expressions for the ablation set-up time, $t_v(r) = \tau e_v / [\alpha F(r)]$, and for the ablation threshold fluence, $F_v = e_v / \alpha$, are valid because the tissue surface remains perpendicular to the laser beam axis until the ablation begins.

A better approximation of the ablation velocity distribution is obtained in the next step by using (5) to approximate the gradient term in (4):

$$\begin{aligned} v_1(r, t) &= \frac{F(r)}{\tau e_v} \left[1 + \left(\frac{\partial x_0(r, t)}{\partial r} \right)^2 \right]^{-\frac{1}{2}} \\ &= \frac{F(r)}{\tau e_v} \left[1 + \left(\frac{\partial F(r)}{\partial r} \frac{t}{\tau e_v} \right)^2 \right]^{-\frac{1}{2}}. \end{aligned} \quad (6)$$

The first-order approximation of the crater profile is then obtained by integrating the ablation velocity v_1 in (6) over time:

$$\begin{aligned} d_1(r) &= \int_{t_v(r)}^{\tau} v_1(r, t) dt \\ &= \frac{F(r)}{F'(r)} \left[\text{Ar sinh} \left(\frac{F'(r)}{e_v} \right) - \text{Ar sinh} \left(\frac{F'(r)}{\alpha F(r)} \right) \right]. \end{aligned} \quad (7)$$

Here, the gradient $(\partial F / \partial r)_r$ is marked by $F'(r)$ for a better clarity of the result.

Finally, accuracy of the crater profile approximation $d_1(r)$ is tested by performing one more step of the iteration procedure. The crater profile evolution $x_1(r, t)$ is calculated first by taking the integral in (7) to a general time t :

$$\begin{aligned} x_1(r, t) &= \int_{t_v(r)}^t v_1(r, t) dt = \frac{F(r)}{F'(r)} \\ &\left[\text{Ar sinh} \left(\frac{F'(r)t}{e_v \tau} \right) - \text{Ar sinh} \left(\frac{F'(r)}{\alpha F(r)} \right) \right]. \end{aligned} \quad (8)$$

Then, its derivative with respect to r is calculated and used to express the second-order estimate of the ablation front velocity $v_2(r, t)$, just as in the previous iteration step (6). Because of the complexity of the obtained expression, its integration to produce the second-order crater profile approximation $d_2(r)$ must be performed numerically for specific fluence profiles of the laser beam.

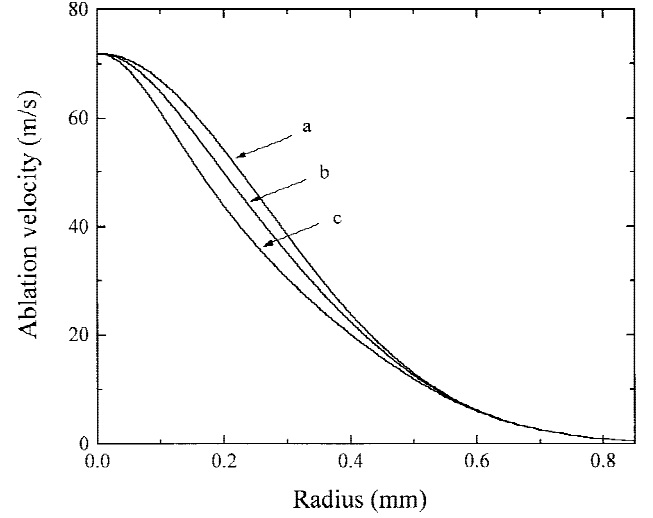


Fig. 2. First-order ablation velocity profiles $v_1(r, t)$ during a 5- μ sec-long temporally constant laser pulse with a Gaussian fluence distribution ($F_0 = 90 \text{ J/cm}^2$). The three curves correspond to times t equal to (a) 1, (b) 3, and (c) 5 μ sec.

NUMERICAL EXAMPLE: THE GAUSSIAN BEAM

The influence of the gradient term in equation (4) on the ablation dynamics is illustrated in Figure 2 by presenting the ablation velocity profile $v_1(r)$ (6) at different times during a 5- μ sec-long temporally constant laser pulse with a Gaussian fluence distribution $F(r) = F_0 \exp(-2r^2/w^2)$. The three plotted curves (Fig. 2, a–c) are calculated at times t equal to 1 μ sec, 3 μ sec, and 5 μ sec, respectively, with the peak fluence $F_0 = 90 \text{ J/cm}^2$. Note that a temporally constant ablation velocity profile, proportional to the (Gaussian) fluence profile, is predicted if the ablation front inclination is neglected in (4).

Convergence of the above presented iteration procedure is analyzed in Figure 3 by comparing the obtained crater profile approximations of the 0th, first, and second orders. The corresponding functions $d_0(r)$ (1), $d_1(r)$ (7), and $d_2(r)$ are plotted in dotted, dashed, and solid lines, respectively. As the results demonstrate, the iteration converges very fast, even at the relatively high peak fluence value of 90 J/cm^2 . The analytically derived crater profile $d_1(r)$ (7), which after inserting the Gaussian fluence profile reduces to

$$\begin{aligned} d_1(r) &= \frac{w^2}{4r} \left[\text{Ar sinh} \left(\frac{4F_0 r}{w^2 e_v} e^{-\frac{2r^2}{w^2}} \right) \right. \\ &\quad \left. - \text{Ar sinh} \left(\frac{4r}{w^2 \alpha} \right) \right], \end{aligned} \quad (9)$$

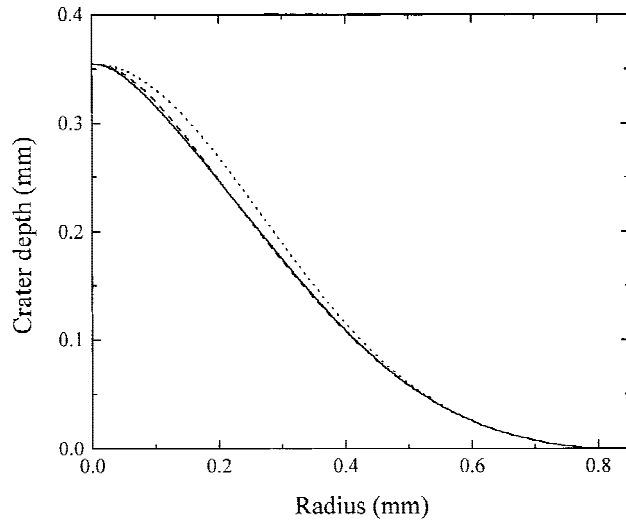


Fig. 3. Comparison of crater profiles as obtained in the 0th (dotted), first (dashed), and second (solid line) orders of the iteration. Peak fluence value equals 90 J/cm^2 .

therefore matches closely the true crater shape, which differs noticeably from the (Gaussian) laser beam fluence distribution.

Figure 4 presents the second-order crater profiles, $d_2(r)$, obtained at equidistant peak fluences from 30 to 150 J/cm^2 . The corresponding 0th order approximations are also plotted for comparison in the left half of the graph (dotted lines). It is apparent that the deviation from the Gaussian profile of the laser beam increases progressively with increasing peak fluence values. Because the maximal crater depth and its surface diameter are not affected by the ablation front inclination effect, it is clear that by assuming the 0th order profile approximation (1), crater volumes at higher pulse fluences are progressively overestimated.

The results shown in Figure 4 indicate a narrow depression evolving along the crater axis at very high pulse fluences. To resolve whether or not this feature is realistic, convergence of the iteration procedure was also checked at the peak fluence value of 150 J/cm^2 (Fig. 5). Because the convergence was found to be nonsatisfying in close proximity to the beam axis, two further iteration steps were performed at this fluence value. To our surprise, the third- and fourth-order profile approximations still differed noticeably at radii below 0.15 mm , indicating that convergence of the iteration in this radius range is indeed very slow at such high fluence (see inset in Fig. 5). There is no doubt, however, that from the radius of approximately 0.15 mm outward, the crater is

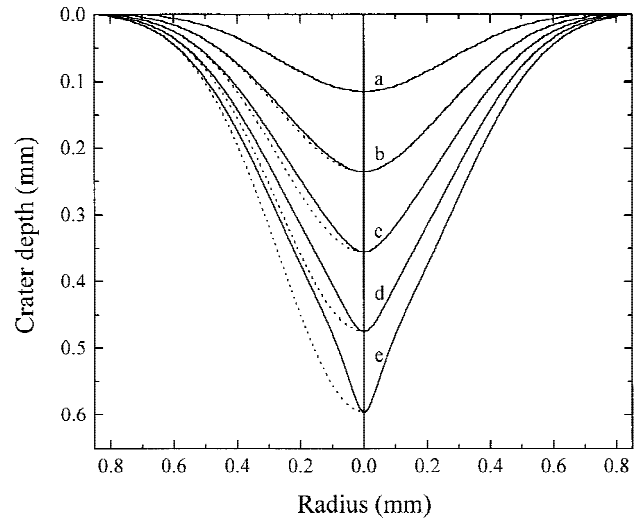


Fig. 4. Second-order crater profile approximations $d_2(r)$ at peak fluence values of (a) 30, (b) 60, (c) 90, (d) 120, and (e) 150 J/cm^2 . The corresponding 0th order approximations $d_0(r)$ (1) are plotted for comparison (dotted lines).

assuming a hornlike conical shape, very similar to the one shown in Figure 4.

DISCUSSION

The inset in Figure 5 shows that, up to the fourth order of approximation, the width of the central depression does not converge toward a finite value. Because the maximal crater depth (at radius $r = 0$) is clearly constant for all iteration orders, a singularity seems to be evolving in the center of the crater. Such behavior could indicate that the iteration procedure is unstable in the discussed radius and fluence range, possibly resulting in profile features that have little in common with exact solution of equation (4) and the actual ablation crater shape.

On the other hand, the emergence of such singularity in predicted crater profiles could be inherent to the dynamical system under consideration. As the crater walls get ever steeper, the ablation velocity namely no longer increases proportionally to the pulse intensity according to (4). Consequently, the crater depth cannot be expected to increase linearly with arbitrarily high peak laser fluences, as predicted by (1). However, with an axially symmetrical fluence distribution (with the radial gradient at $r = 0$ equal to 0), crater bottom on the beam axis is always exactly perpendicular to the beam axis from the symmetry reasons. At this singular point, the one-dimensional approximation (2) should thus hold

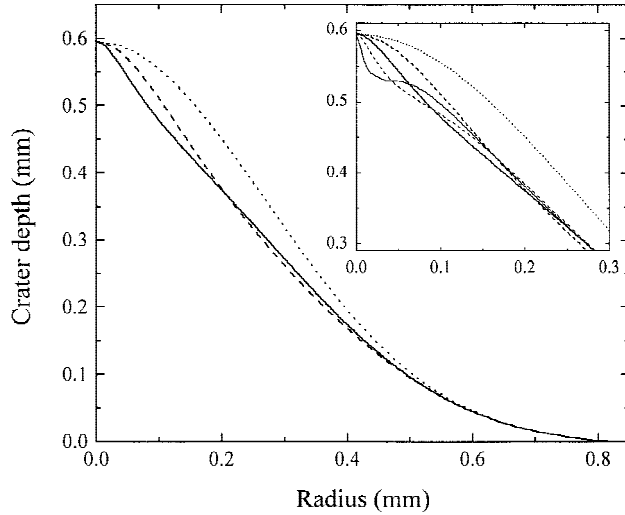


Fig. 5. Comparison of crater profile approximations of the 0th (dotted), first (dashed), and second (solid line) orders, obtained at peak fluence value of 150 J/cm^2 . The third- and fourth-order approximations are plotted in the inset and show the central part of the crater (thin dashed and thin solid line, respectively).

exactly for arbitrarily high fluences, whereas the ablation process elsewhere in the crater gradually stalls, possibly forming a secondary crater bottom at a lower depth (see the inset in Fig. 5). In an experimental situation, we may expect the presence of beam wondering, imperfect axial symmetry of the beam intensity distribution, and inhomogeneity of the target tissue to preclude observation of such singularity in the crater profiles.

Whereas our model treats only the effect of a single laser pulse, sequences of repetitive laser pulses are often used to increase the ablation effect. In the experiments quoted above [1], for example, 10 pulses were applied to each point on the tissue surface at a repetition rate of 1 Hz. Such a low repetition rate ensures a complete dissipation of heat from the interaction volume, so that successive macropulses act independently on thermally relaxed tissue [5,9]. In a sequence of n pulses, the ablation threshold fluence F_v is thus delivered n times without inducing any ablation effect, in contrast with the single-pulse irradiation case, where the same amount of pulse fluence is lost just once. The pulse fluence F that causes the same ablation effect as a sequence of n pulses with a single-pulse fluence F_n can therefore be estimated as

$$F = nF_n - (n - 1)F_v. \quad (10)$$

By using $F_v = e_v/\alpha = 1.2 \text{ J/cm}^2$, it follows that our

calculation with the peak fluence of 30 J/cm^2 corresponds to a sequence of 10 pulses with the peak fluence equal to 4.1 J/cm^2 .

Note that equation (10) can only be used when the crater walls are gently sloped, so that the influence of the ablation front inclination is negligible. Even then, the crater diameter, obtained with a sequence of laser pulses, will always be smaller than with a single pulse of correspondingly higher fluence. The final crater diameter is given by the radius, at which the pulse fluence equals the ablation threshold fluence (see equation (1)). In a low-repetition-rate sequence, when the irradiated tissue is cooled down between successive pulses, this condition must be met with each pulse independently. This results in a lower crater diameter, and the crater shapes in the two cases would thus inevitably differ. Strictly speaking, the relation (10) holds exactly only for the one-dimensional ablation geometry, but it can also be used for relating the maximal crater depths, especially with fluence profiles and intensities that result in craters with relatively flat bottoms.

The experimentally obtained crater depth versus fluence dependence in [1] was assumed to be linear, with no saturation due to debris screening. This assumption was supported by relating the applied fluences ($F_0 \leq 4 \text{ J/cm}^2$) to experimental results from CO_2 laser ablation of bone by Forrer et al. [10]. However, even though the absorption coefficients of the two tissues at the two respective wavelengths may be similar, such argumentation is not valid because of the much longer pulse duration ($\tau = 150 \text{ } \mu\text{sec}$) of the CO_2 laser used in [10]. As we have demonstrated recently [4], the debris screening process is governed by the radiation intensity, which results in a strong influence of the pulse duration on the ablation dynamics. In the experiment under consideration, each FEL fluence thus corresponds to approximately 30 times higher CO_2 laser fluence. Consequently, a marked deviation from a linear crater depth versus fluence relationship can be expected.

In conclusion, the ablation crater shapes can differ noticeably from the fluence profile of the laser pulse. The effect, which results from inclination of the ablation front due to spatial nonhomogeneity of the laser beam intensity, increases progressively with increasing pulse fluences. Solutions of the derived ablation dynamics model can be found for moderate peak fluence values by

using an iterative procedure, as is presented for the case of the temporally constant Gaussian beam. Further work is needed to investigate the source and consequences of the observed instability, including the effects of repetitive-pulse sequences, and treat the interplay with debris screening.

REFERENCES

1. Ostertag M, McKinley JT, Reinisch L, Harris DM, Tolk NH. Laser ablation as a function of the primary absorber in dentin. *Lasers Surg Med* 1997; 21:384–394.
2. Hibst R, Keller U. Experimental studies of the application of the Er:YAG laser on dental hard substances: I. Measurement of the ablation rate. *Lasers Surg Med* 1989; 9:338–344.
3. Izatt JA, Sankey ND, Partovi F, Fitzmaurice M, Rava RP, Itzkan I, Feld MS. Ablation of calcified biological tissue using pulsed hydrogen fluoride laser radiation. *IEEE J Quant Electr* 1990; 26:2261–2270.
4. Majaron B, Šušterčič D, Lukač M, Skalerič U, Funduk N. Heat diffusion and debris screening in Er:YAG laser ablation of hard biological tissues. *Appl Phys B* 1998; 66:479–487.
5. Walsh JT, Deutsch TF. Er:YAG laser ablation of tissue: measurement of ablation rates. *Lasers Surg Med* 1989; 9:327–337.
6. Walsh JT, Deutsch TF. Pulsed CO₂ laser ablation of tissue: effect of mechanical properties. *IEEE Trans Biomed Engin* 1989; 36:1195–1201.
7. Domankewitz Y, Nishioka NS. Measurement of laser ablation threshold with a high-speed framing camera. *IEEE J Quant Electr* 1990; 26:2276–2278.
8. LeCarpentier GL, Motamedi M, McMath LP, Rastegar S, Welch AJ. Continuous wave laser ablation of tissue: analysis of thermal and mechanical events. *IEEE Trans Biomed Engin* 1993; 40:188–200.
9. Fried D, Visuri SR, Featherstone JDB, Walsh JT, Seka W, Glena RE, McCormack SM, Wigdor HA. Infrared radiometry of dental enamel during Er:YAG and Er:YSGG laser irradiation. *J Biomed Optics* 1996; 1:455–465.
10. Forrer M, Frenz M, Romano V, Altermatt HJ, Weber HP, Silenok A, Istomyn M, Konov VI. Bone-ablation mechanism using CO₂ lasers of different pulse duration and wavelength. *Appl Phys B* 1993; 56:104–112.